Since January 2020 Elsevier has created a COVID-19 resource centre with free information in English and Mandarin on the novel coronavirus COVID-19. The COVID-19 resource centre is hosted on Elsevier Connect, the company's public news and information website.

Journal of Molecular Graphics and Modelling 107 (2021) 107969

Contents lists available at ScienceDirect

Journal of Molecular Graphics and Modelling

journal homepage: www.elsevier.com/locate/jmgm

Multifunctional inhibitors of SARS-CoV-2 by MM/PBSA, essential dynamics, and molecular dynamic investigations

K. Amith Kumar, Monica Sharma, Vikram Dalal, Vishakha Singh, Shailly Tomar, Pravindra Kumar *

Department of Biosciences and Bioengineering, Indian Institute of Technology Roorkee, 247667, India

ARTICLE INFO

Keywords:
SARS-CoV-2
Triterpenoids
Cytokine storm
RNA-Dependent RNA polymerase
Papain-like protease
Main protease

ABSTRACT

The ongoing COVID-19 pandemic demands a novel approach to combat and identify potential therapeutic targets. The SARS-CoV-2 infection causes a hyperimmune response followed by a spectrum of diseases. Limonoids are a class of triterpenoids known to prevent the release of IL-6, IL-15, IL-1α, IL-1β via TNF and are also known to modulate PI3K/Akt/GSK-3β, JNK1/2, MAPKp38, ERK1/2, and PI3K/Akt/mTOR signaling pathways and could help to avoid viral infection, persistence, and pathogenesis. The present study employs a computational approach of virtual screening and molecular dynamic (MD) simulations of such compounds against RNA-dependent RNA polymerase (RdRp), Main protease (Mpro), and Papain-like protease (PLpro) of SARS-CoV-2. MD simulation, Molecular Mechanics Poisson-Boltzmann Surface Area (MM/PBSA), and Essential dynamics revealed that the macromolecule-ligand complexes are stable with very low free energy of binding. Such compounds that could modulate both host responses and inhibit viral machinery could be beneficial in effectively controlling the global pandemic.

1. Introduction

Covid-19 is caused by a recently discovered coronavirus SARS-CoV-2. SARS-CoV-2 emerged in Wuhan, China, belongs to the Coronaviridae family [1]. These are spherically enveloped particles, enclosed within a nucleocapsid containing a large single-stranded positive-sense RNA [2]. These viruses are known to infect both avian and mammalian species [2]. There are seven variants of coronaviruses that are known to infect humans: HCoV-229E, HCoV-NL63, HCoV-OC43, HCoV-HKU1, SARS-CoV-1, MERS-CoV, and SARS-CoV-2 [3]. These viruses are rapidly evolving because of their high recombination rates and some of them are highly pathogenic and well capable of causing a global pandemic [4,5].

Most of the people with COVID-19 remain asymptomatic or develop mild symptoms, about 10–20% (especially older people, those with compromised immune system, people under medical intervention) develop a spectrum of symptoms of pneumonia, acute respiratory distress syndrome (ARDS), sepsis, intravascular coagulation, lung fibrosis, multiorgan failure, and death in a few cases [6–8]. As the hyperimmune response is the primary reason for the lethality caused by SARS-CoV-2, immune-modulation is a highly potent therapeutic target in COVID-19 disease progression [9–11]. In this context, the anti-inflammatory properties of limonoids are well studied [12,13]. Limonoids are a class of tetranortriterpenoids and have recently been identified for their wide range of biological activities, including anticancer, antibacterial, antifungal, insecticidal, antidiabetic, antimalarial, and antiviral activities, and also as immunomodulators [14–17]. Oleanolic acid, Azadirachtins, and other Triterpenoids can inhibit Cathepsin-L, a protease involved in processing Spike glycoprotein of SARS-CoV-2 (Fig. 1) [18–20]. Most of the Limonoids (Azadirachtins, Epoxyazadiradione, and Nomilin) extracted from leaves of neem and lemon seeds are reported to prevent the activation of the tumor necrosis factor (TNF via TNFR1 and TNFR2), NF-κB, and COX-2 [21]. Thereby preventing the release of interleukin IL-6, IL-1α, IL-1β, IL-15 (Fig. 2). Azadirachtins have been shown to inhibit the pro-inflammatory response through a novel pathway, which could be beneficial in combating inflammatory responses [21,22].

The persistent infection of SARS-CoV is established through JNK, PI3K/Akt/GSKβ, and p38 MAPK signaling pathways [23,24]. Upon infection with SARS-CoV, a cascade of signaling pathways including, c-Jun N-terminal protein kinase JNK and PI3K/Akt/GSKβ, Mitogen-activated protein kinases (MAPK), extracellular signal-related kinase (ERK) 1/2, and p38 MAPK are phosphorylated expressing Bcl-2 and Bcl-xL preventing the apoptosis of the infected cells [25–27]. Nucleocapsid (N) protein plays an

* Corresponding author.
E-mail addresses: pravindra.kumar@bt.iitr.ac.in, pravinmcu@gmail.com (P. Kumar).

https://doi.org/10.1016/j.jmgm.2021.107969
Received 18 March 2021; Received in revised form 15 June 2021; Accepted 15 June 2021
Available online 17 June 2021

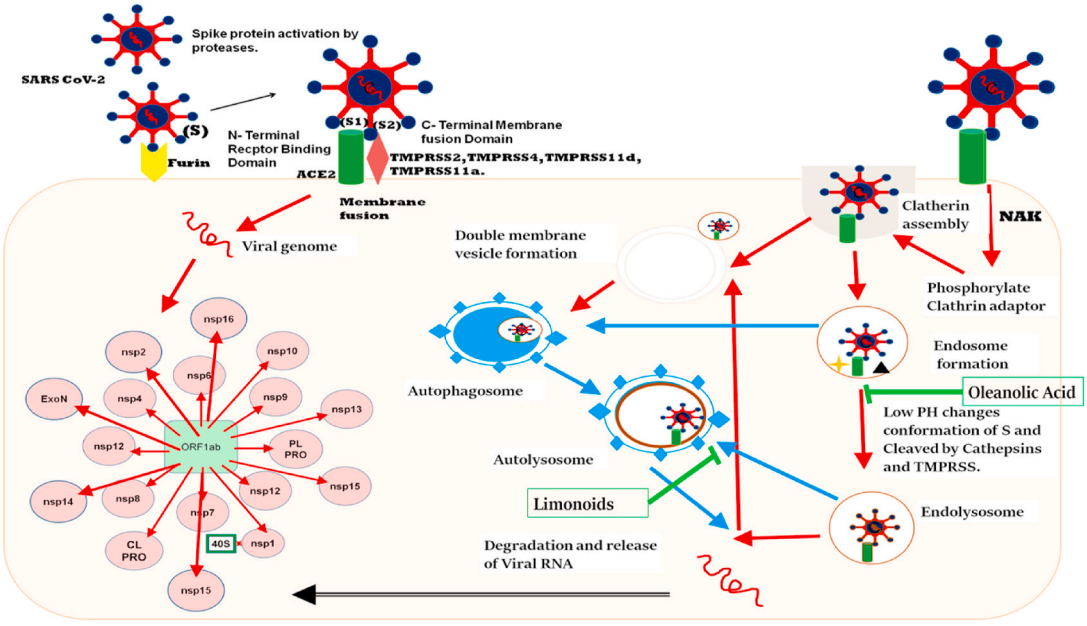

Fig. 1. Mode of Entry of SARS-CoV-2 and inhibition by triterpenoids: SARS-CoV-2 is believed to enter via endosomal dependent and independent pathways. While the main mode of entry is by clatherin mediated endocytosis followed by the formation of double-membrane vesicles and autophagy. Triterpenoids like oleanolic acid are known to inhibit Cathepsin-L and like chloroquine, some limonoids are known to inhibit Autophagy.

important role in the phosphorylation of Akt and JNK, which in turn is phosphorylated by GSK3 [28]. Inhibitors of Akt and JNK, lead to the apoptotic death of the infected cells and, inhibition of GSK3 was shown to inhibit viral replication [28]. Limonoids from neem extracts (nimbolide), *Withania somnifera* (Withaferin A), and citrus limonoid glucosides are known to inhibit cytoprotective autophagy and promote apoptosis of infected cells by modulating PIK3/Akt/GSK-3β, p38 MAPK, JNK1/2, and ERK ½, signaling pathways [21,29,30] (Fig. 3). Therefore, such compounds may prove to be potential anti-coronaviral compounds to tackle the persistent infection and replication of SARS-CoV-2 by promoting apoptosis of infected cells.

RNA viruses are prone to high mutation rates, this drives genome variability leading to the evolution of viruses capable of immunoevasion [8]. The genome of human corona-viruses is highly similar to the corona-viruses found in other organisms [31]. The high mutation rates and high recombination rates, increases the risk of animal-human transmission and also increases the possibility of the emergence of more pathogenic variants of the virus in the future [8,32,33]. Whereas host proteins are evolutionarily conserved, and viruses depend on these proteins for infection, multiplication, and pathogenesis. Thus, targeting host proteins involved in viral replication or virus-derived host response are potential therapeutic candidates, and the compounds that could modulate both the host response and target viral duplication machinery could be important to control the global pandemic effectively.

We commenced our study by investigating the mechanism of infection, propagation and, pathogenesis of coronaviruses. Then, compounds of plant origin with potential anti-inflammatory properties, inhibit cytoprotective autophagy and promote apoptosis of infected cells were identified with the aid of literature. These compounds are reported to modulate PI3K/Akt/GSK-3β, JNK1/2, MAPKp38, ERK1/2, and PI3K/Akt/mTOR signaling pathways, Which are critical for the establishment of covid-19. The identified compounds belonged to a class of triterpenoids called limonoids. Later these compounds (azadirachtins and ceramicines) and structurally similar steroidal lactones called withanolides were screened for their therapeutic

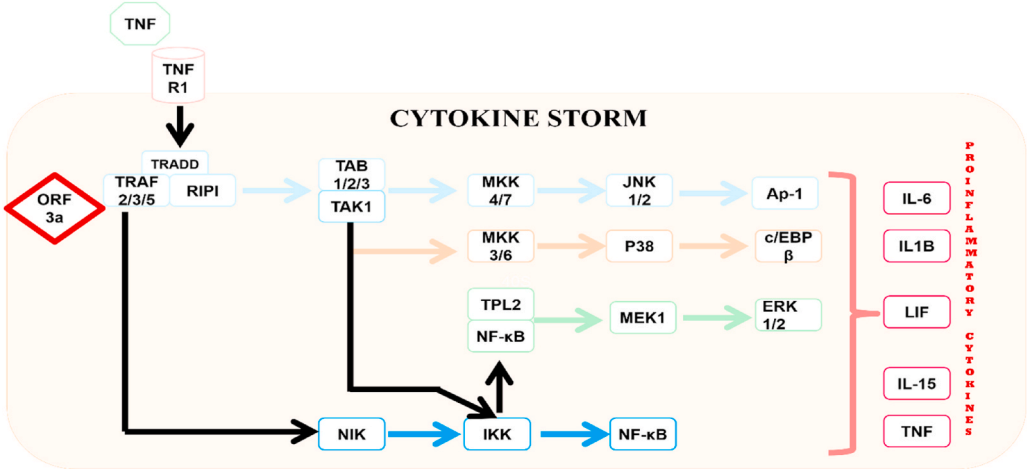

Fig. 2. TNF signaling pathway and Limonoids: Limonoids are known to prevent the release of proinflammatory cytokines via Nf-κB, JNK1/2, P38, and ERK1/2 signaling pathways.

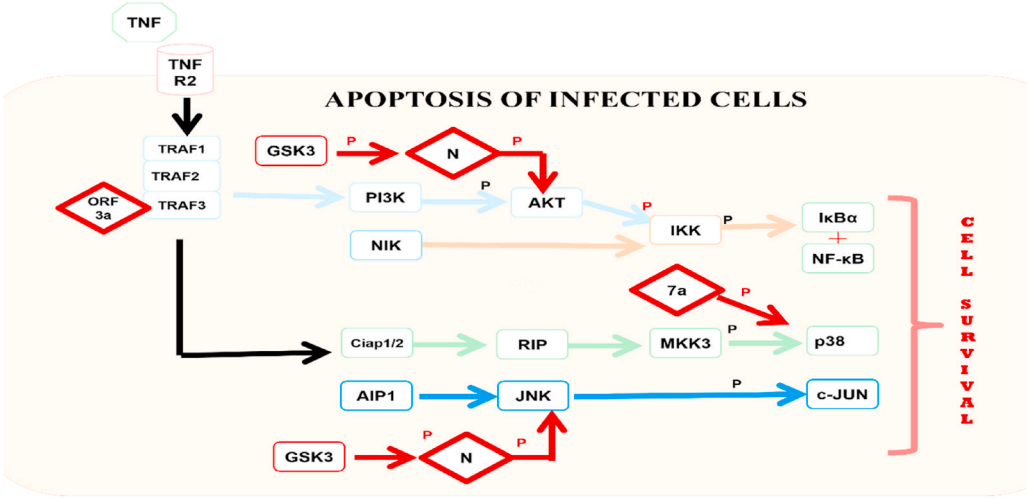

Fig. 3. PI3K-AKT signaling pathway: SARS-CoV-2 prevents the apoptosis of infected cells by phosphorylation of AKT/JNK by N-protein and p38 by 7a. Limonoids are known to promote apoptosis of infected cells by modulating Nf-κB, and AKT/JNK/p38 pathways.

potential against the SARS-CoV-2 main duplication machinery RdRp, Mpro, and PLpro using Autodock Vina module of PyRx 0.8 [34]. The compounds that returned good binding affinity were re-docked and re-scored using Autodock [35]. The protein-ligand complexes with the best free energy of binding were subjected to Molecular Dynamic (MD) simulations, essential dynamics, and Molecular Mechanic/Poisson-Boltzmann Surface Area (MM/PBSA) to investigate the structural dynamics, stability, and binding affinity. The 2D structures of the top hits are included in Table 1.

2. Methods

2.1. Virtual screening

PyRx is a virtual screening tool with an inbuilt OpenBabel module for ligand processing and AutoDock Vina module for docking and scoring. The 3D conformers of ligands were downloaded from the ChEBML database [ChEMBL: a large-scale bioactivity database for drug discovery] and loaded in PyRx using the OpenBabel module. The conjugate gradient algorithm was implied for energy minimization using Universel Force Field (UFF). The energy minimized structures were converted to pdbqt format. The SARS-CoV-2 RdRp in complex with cofactors (PDB ID: 6M71) was prepared by removing the cofactors (nsp 7 & nsp 8) and remodelling nsp 12 using swiss model portal and 6M71 as template [36]. Crystal structure of Mpro (PDB ID: 6LU7) was prepared by removing waters and the ligand N3. PLpro (PDB ID: 6W9C) was downloaded from the PDB database and was prepared for docking by removing the heteroatoms and extra chains from the structure [37,38]. The grid box dimensions and center points of RdRp, PLpro, and Mpro are mentioned in Table S1. Total 9 different docking poses were generated and analyzed based on the interactions and the binding affinity with protein.

2.2. Molecular docking

AutoDock Tools was used for molecular docking of azadirachtins, ceramicines, and withanolides with RdRp, Mpro, and PLpro [35]. The hydrogen atoms and gasteiger charges were added and saved in pdbqt format. The molecular grid was set in between motif A (612–626) and motif G (499–511) covering the catalytic core of RdRp [39]. For PLpro the grid was set around the S3 and S4 pocket that opens into the active site. For Mpro the grid was set in between domains 1 and 2 covering the catalytic dyad of His41 and Cys145 [40]. The details of the grid are mentioned in Table S1. The Lamarckian genetic algorithm was used to generate 25 docked conformations of each ligand. The results were analyzed using the Discovery studio visualizer [41].

Table 1
2D structures of lead molecules selected for molecular simulation studies.

S.No.	ChEMBL id	2D Structure
1.	CHEMBL502955	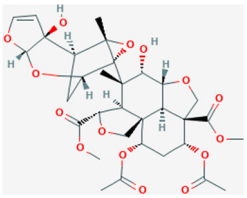
2.	CHEMBL2335028	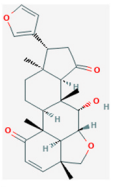
3.	CHEMBL4215430	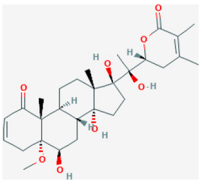
4.	CHEMBL2288848	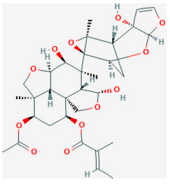
5.	CHEMBL2335026	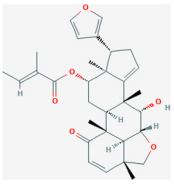
6.	CHEMBL488913	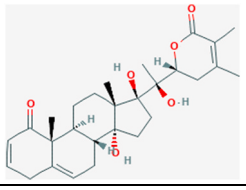

Table 2
Virtual screening and Molecular docking of azadirachtins, ceramicines, and withanolides with SARS-CoV-2 RNA dependent RNA polymerase (RdRp), Main protease (Mpro), and Papain-like protease using PyRx and AutoDock Tools.

S.No.	CHEMBL id	Common Name	AutoDock Vina (kcal/mol)	AutoDock Tools (kcal/mol)	Estimated Ki
1.	RdRp-CHEMBL502955	Azadirachtin-Q	−8.3	−10.4	22.01 nM
2.	RdRp-CHEMBL508913	Azadirachtin-M	−8.0	−10.7	14.72 nM
3.	RdRp-CHEMBL2288846	Azadirachtin-B	−7.8	−10.4	22.01 nM
4.	RdRp-CHEMBL2335024	Ceramicine-F	−8.8	−9.8	66.85 nM
5.	RdRp-CHEMBL2335026	Ceramicine-H	−8.2	−10.9	9.92 nM
6.	RdRp-CHEMBL2335028	Ceramicine-J	−7.8	−8.2	1.06 μM
7.	RdRp-CHEMBL515208	Ceramicine-B	−8.0	−13.7	89.03 pM
8.	RdRp-CHEMBL4211870	Withanolide	−8.6	−10.7	13.42 nM
9.	RdRp-CHEMBL4211019	Withanolide	−8.4	−10.9	10.19 nM
10.	RdRp-CHEMBL4215430	Withanolide	−8.3	−8.7	452.26 nM
11.	RdRp-CHEMBL1097107	Withanolide	−8.4	−10.9	10.32 nM
12.	Mpro-CHEMBL506084	Azadirachtin-A	−8.2	−12.3	919.71 pM
13.	Mpro-CHEMBL502955	Azadirachtin-Q	−7.3	−13.2	213.39 pM
14.	Mpro-CHEMBL2272994	Azadirachtin-H	−7.5	−13.0	307.24 pM
15.	Mpro-CHEMBL2288847	Azadirachtin-D	−7.1	−12.2	1.12 nM
16.	Mpro-CHEMBL2335027	Ceramicine-I	−7.6	−11.2	6.62 nM
17.	Mpro-CHEMBL2335028	Ceramicine-J	−9.2	−11.3	5.0 nM
18.	Mpro-CHEMBL2335026	Ceramicine-H	−7.6	−13.2	218.05 pM
19.	Mpro-CHEMBL457896	Ceramicine-A	−7.9	−10.5	19.37 nM
20.	Mpro-CHEMBL4215430	Withanolide	−7.0	−9.0	257.64 nM
21.	Mpro-CHEMBL2333675	Withanolide	−8.4	−13.8	71.14 pM
22.	Mpro-CHEMBL4288984	Withanolide	−8.3	−12.2	1.07 nM
23.	PLpro-CHEMBL2272994	Azadirachtin-H	−7.2	−11.2	6.54 nM
24.	PLpro-CHEMBL2288848	Azadirachtin-I	−7.9	−10.6	15.69 nM
25.	PLpro-CHEMBL502955	Azadirachtin-Q	−6.5	−9.4	132.37 nM
26.	PLpro-CHEMBL509309	Azadirachtin	−6.9	−9.0	264.67 nM
27.	PLpro-CHEMBL515521	Ceramicine-D	−7.9	−10.0	45.31 nM
28.	PLpro-CHEMBL2335026	Ceramicine-H	−7.4	−9.4	136.83 nM
29.	PLpro-CHEMBL2335027	Ceramicine-I	−7.6	−9.5	116.86 nM
30.	PLpro-CHEMBL1222037	Withanolide	−8.4	−10.1	40.44 nM
31.	PLpro-CHEMBL4288984	Withanolide	−8.3	−10.6	17.66 nM
32.	PLpro-CHEMBL488913	Withanolide	−7.8	−7.6	2.45 μM
33.	PLpro-CHEMBL4211870	Withanolide	−7.6	−6.2	30.32 μM

2.3. Molecular dynamic simulations

The molecular dynamics simulations were performed to explore the structural and conformational stability of protein and protein-ligand complexes. These macromolecules were subjected to molecular dynamics using the GROMOS96 43a1 force field in GROMACS 2019.5 and the topology of the ligands was generated using PRODRG online server [42–45]. The systems were solvated using simple point charge (SPC) water model in a cubic box with a minimum distance of 1 nm from the edge of the protein. The counterions $13Na^{+}$, $4Na^{+}$and $3Cl^{-}$ were added to RdRp, Mpro and PLpro respectively; to maintain the overall neutrality of the system. The steric clashes were dealt with the steepest descent minimization algorithm, carried for 50,000 steps with a maximum force of 10 $kJmol^{-1}$. The systems were equilibrated using NVT and NPT for 100 ps of position restrain. Periodic boundary conditions were employed at a constant temperature of 300 K and 1 atm pressure using the V-rescale temperature coupling method and Parrinello-Rahman coupling method, respectively. The Particle Mesh Ewald method was used for computing the long-range electrostatic interactions [46]. Finally, the leap-frog algorithm was employed to carry out the 50 ns of production dynamics for the equilibrated system [47]. The generated trajectories were used to monitor the structural deviations and fluctuations of the protein and protein-ligand complexes [48,49]. Linear Constraint Solver (LINCS) algorithm was used to constrain the bond lengths of heavy atoms [50]. The short-range forces were calculated with a minimum cutoff set to 1.2 nm using verlet cutoff scheme [51]. The relative root mean square deviation (RMSD) with respect to the initial reference trajectory was calculated using g_rms. The flexibility of the Cα backbone atoms of each residue of native proteins, and in complex with ligands were studied through the root mean square fluctuations (RMSF) using g_rmsf. These values were further compared with the RMSF calculated from the experimental B-factor values [52]. The g_hbond tool in GROMACS was used to calculate the number of hydrogen bonds between the protein-ligand complexes during the 50 ns of molecular simulation.

2.4. Essential dynamics

The relative conformational dynamics and atomic fluctuations of the functionally relevant substructures in the native and ligand-bound forms were studied using PCA [53,54]. The trajectories generated during the molecular dynamics simulation of 50 ns were used for PCA analysis. A cross-correlation matrix was developed by removing the translational and rotational movements and monitoring the relative Cα backbone atomic fluctuations. The generated eigenvalues represent the energetic contribution from the corresponding principal component (PC), while the vector represents the direction of motion. The projected eigenvalues and eigenvectors were analyzed to determine the overall flexibility of protein.

2.5. Binding free energy calculations using MM/PBSA

Molecular Mechanics Poisson-Boltzmann Surface Area (MMPBSA) was used to calculate the free energy of binding (ΔG) of a small molecule bound to a macromolecule using g_mmpbsa. ΔG is calculated based on the difference in free energy between bound ligand-macromolecule complex and the ligand and macromolecule in the unbound state, as:

$$\Delta G = (G_{\text{Ligand-Macromolecule}}) - G_{\text{Ligand}} - G_{\text{Macromolecule.}}$$

MM/PBSA was performed over a total of 1000 snapshots, generated at every 10 ps from the final 10 ns of molecular dynamics using a one step calculation method as described earlier [55–57].

3. Results

3.1. Virtual screening

Virtual screening of azadirachtins, ceramicines, and withanolides were done against RdRp, PLpro, and Mpro. In RdRp, AutoDock Vina results showed that all the screened molecules bind in a similar mode with a binding affinity in the range of −8.6 to −7.8 kcal/mol (Table 2). Screened azadirachtins, ceramicines, and withanolides bound at the substrate-binding pocket of Mpro with a binding affinity of −9.2 to −7.0 kcal/mol (Table 2). The compounds were estimated to bind within the S3-S4 subsites of SARS-CoV-2 PLpro. The binding affinity of ligands with PLpro is mention in Table 2. Three molecules from each class exhibit the highest binding affinities with macromolecules were considered for molecular docking.

3.2. Molecular docking

Molecular docking of screened compounds with protein receptors was done using AutoDock Tools. Molecular docking results illustrated that ligands bound at the active site involved Lys545, Arg553, Arg555, Asp623, Asp760, and Asp761 residues of RdRp with a binding affinity in the range of that −13.7 to −8.7 kcal/mol, as shown in Fig. 4 and Table 2. Fig. 5 shows that azadirachtin, ceramicine, and withanolide interact with the catalytic triad (His41 Cys145 and Gln189) of Mpro. The other residues such as Thr24, Thr25, Thr26, Cys 44, Thr45, Ser 46, Met49, Leu 141, Asn 142, Gly 143, Ser 144, His 164, Met 165, Glu 166, Arg 188, Thr190 also played a major role in the binding of ligands with Mpro [40, 58]. CHEMBL2333675 (withanolide) and CHEMBL457896 (ceramicine-A) predicted the highest and least binding affinity of −13.8 and −10.5 kcal/mol, respectively, as shown in Table 2. Azadirachtin, ceramicine, and withanolide bind with amino acid residues (Trp 106,

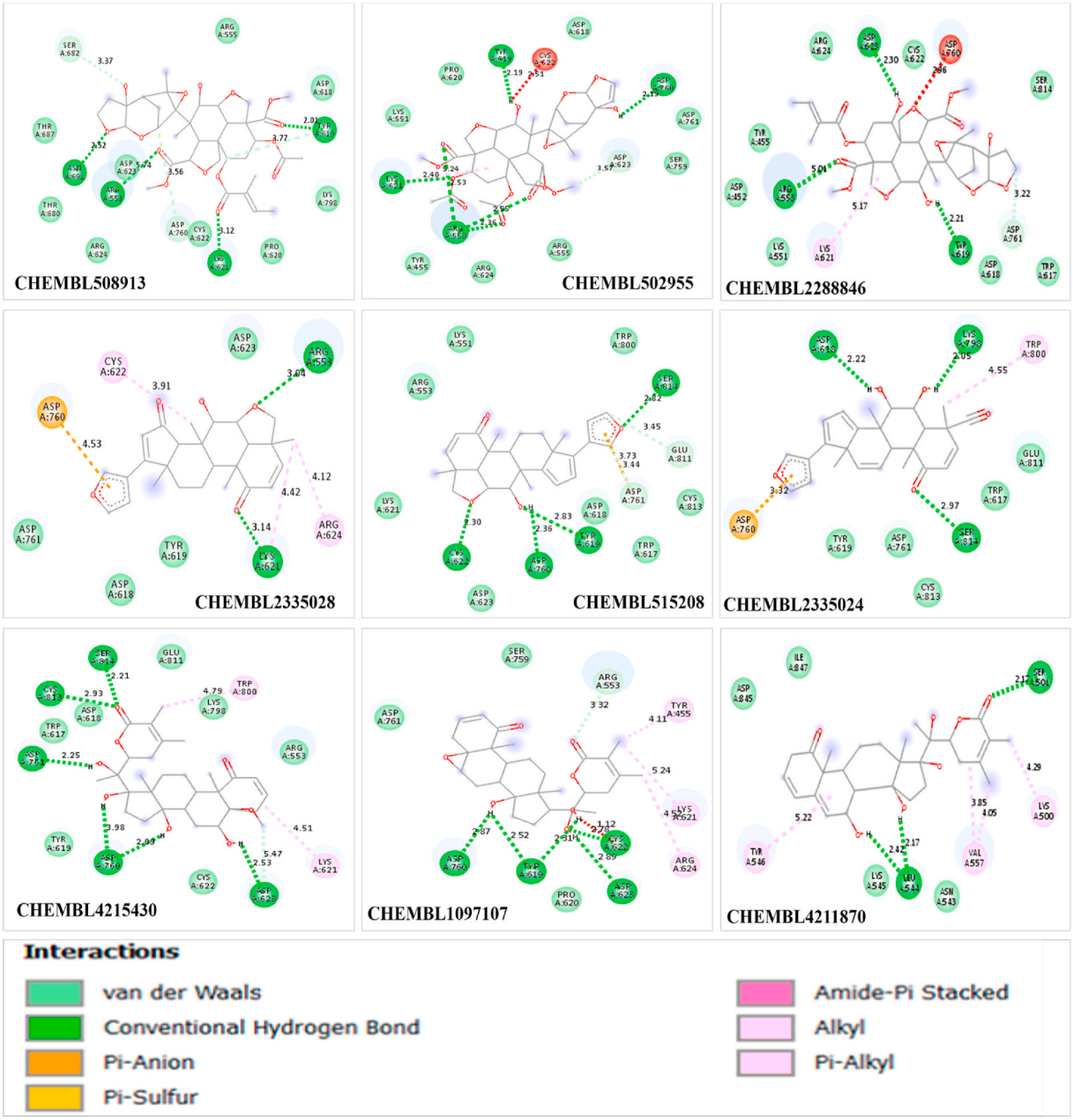

Fig. 4. The predicted binding mode of ligands with RNA Dependent RNA Polymerase (RdRp). 2D representation of the molecular interactions of azadirachtins, ceramicines, and withanolides with RdRp.

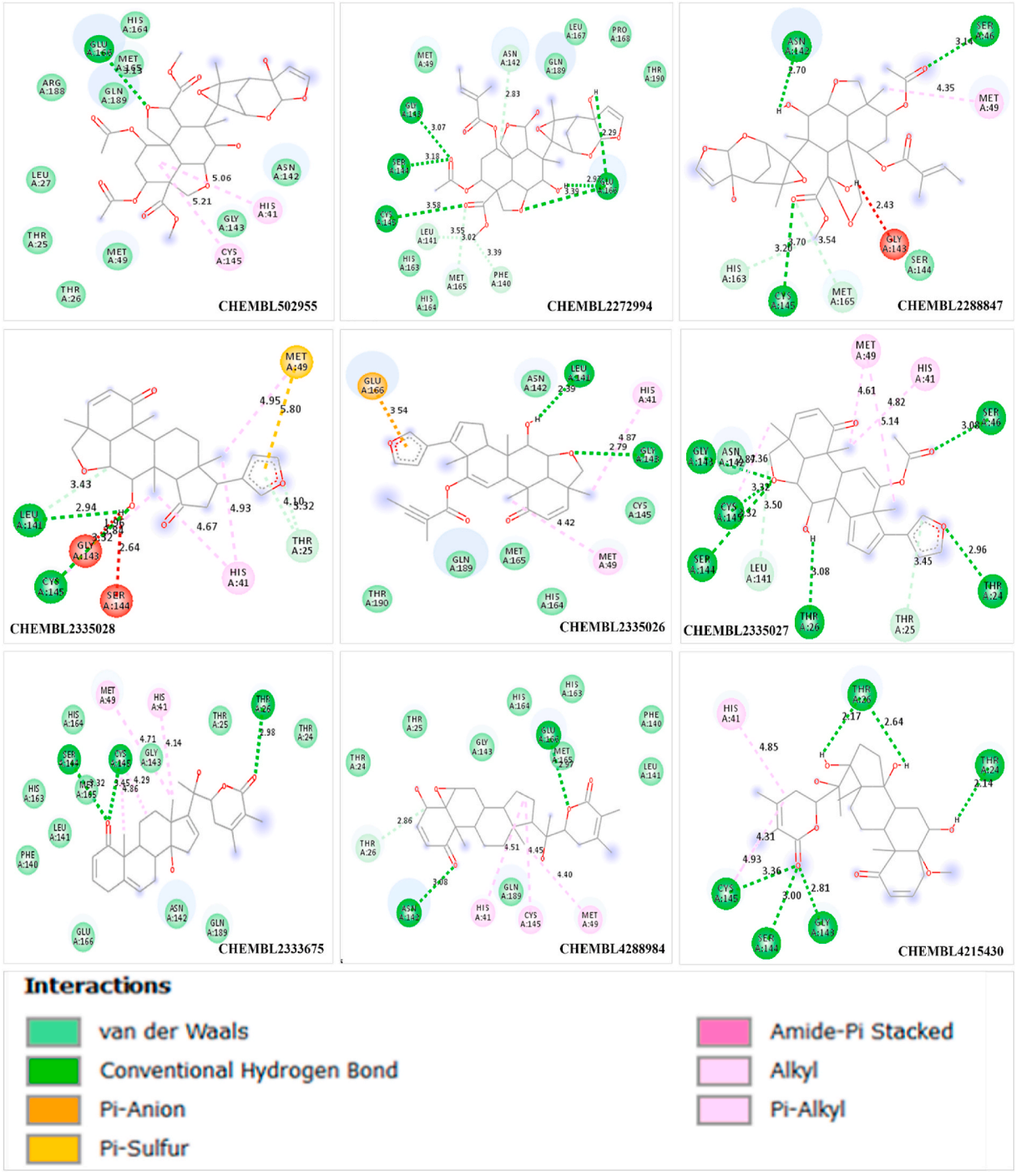

Fig. 5. 2D representation of interactions between azadirachtin, ceramicine, and withanolide with Mpro.

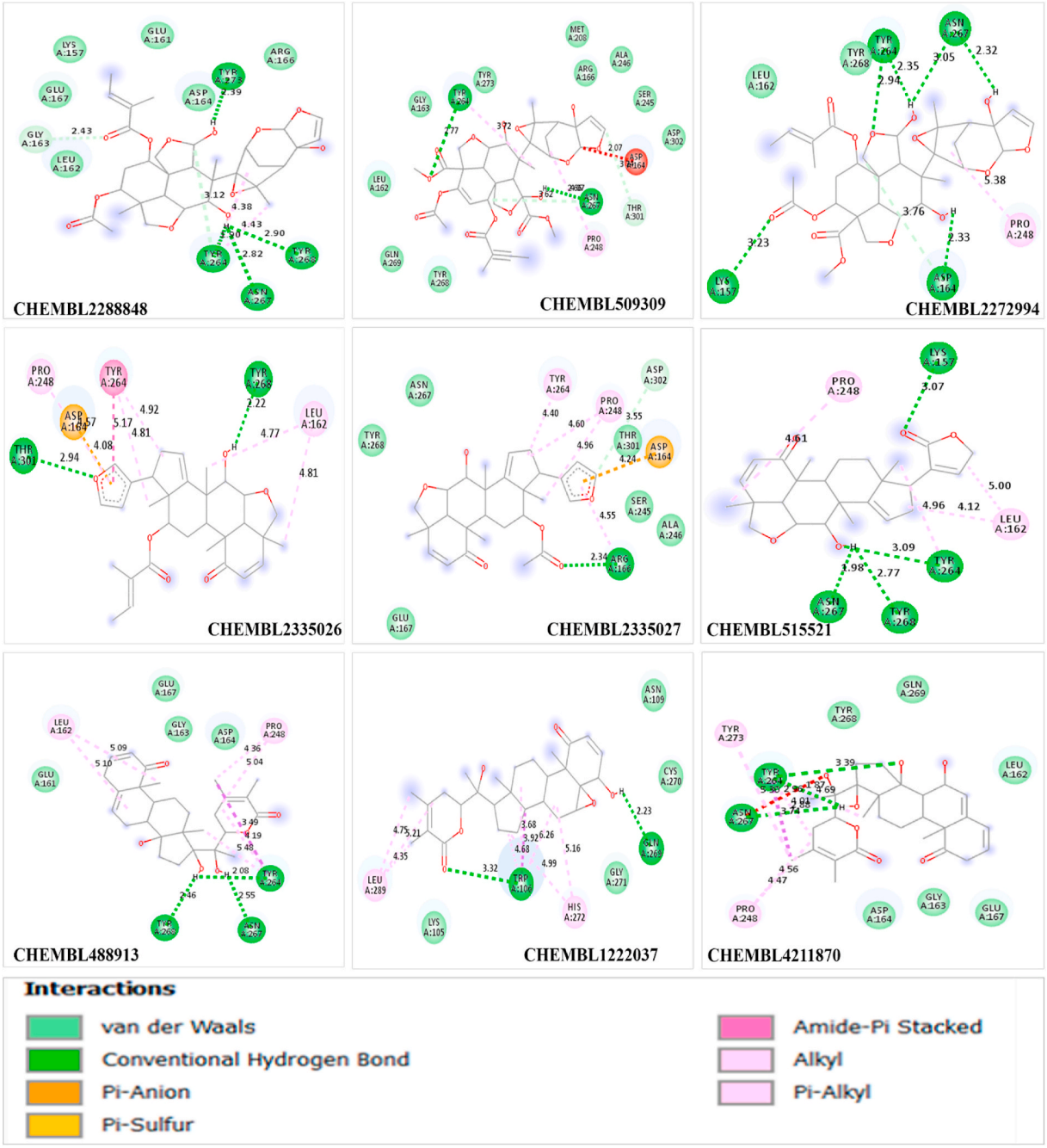

Fig. 6. Docking interactions analysis of ligands with Papain like protease (PLpro). 2D illustrative representation of azadirachtins, ceramicines, and withanolides with PLpro.

Lys 157, Leu 162, Gly 163, Asp 164, Arg 166, Glu 167, Pro247, Pro248, Tyr264, Tyr267, Tyr268, Tyr273, Thr301, and Thr302) of PLpro, as shown in Fig. 6. In Table 2, it can be seen that all the ligands with PLpro exhibit binding affinity in the range of −11.2 to −6.2 kcal/mol. Overall, molecular docking results suggested that azadirachtin, ceramicine, and withanolide can bind with a considerable binding affinity at the critical sites of RdRp, Mpro, and PLpro.

3.3. Molecular dynamics results

3.3.1. RMSD analysis

The RMSD plot shows that the RdRp-CHEMBL502955, RdRp-CHEMBL2335028, and RdRp-CHEMBL4215430 complexes are comparatively more stable with an average deviation of 0.35 nm, 0.41 nm, and 0.37 nm, respectively (Fig. 7A). The Apo-RdRp had an average RMSD of 0.46 nm with deviations not exceeding 0.6 nm (Table 3). Apo-Mpro had a steady run with an RMSD ranging between 0.2 and 0.35 nm

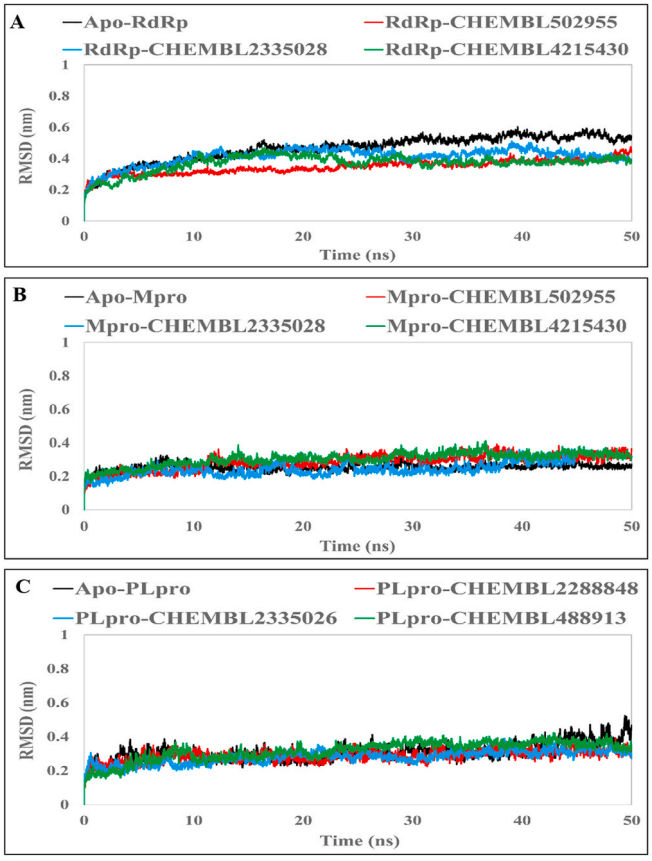

Fig. 7. Root mean square deviation (RMSD) plots of RdRp, Mpro, and PLpro in apo forms, and with ligand-bound for the molecular simulation of 50 ns. A) Apo-RdRp, RdRp-CHEMBL502955, RdRp-CHEMBL2335028, and RdRp-CHEMBL4215430 complexes; B) Apo-Mpro, Mpro-CHEMBL502955, Mpro-CHEMBL2335028, and Mpro-CHEMBL4215430 complexes; and C) Apo-PLpro, PLpro-CHEMBL228848, PLpro-CHEMBL2335026, and PLpro-CHEMBL488913 complexes.

Table 3
The average RMSD and RMSF of the protein-ligand complexes for the duration of molecular simulation of 50 ns.

S.No.	Macromolecule	Average RMSD (nm)	Average RMSF (Å)	Average no. of H-bond
1	Apo-RdRp	0.46	1.7	
2	RdRp-CHEMBL502955	0.35	1.5	4.55
3	RdRp- CHEMBL2335028	0.41	1.5	1.52
4	RdRp- CHEMBL4215430	0.37	1.6	2.68
5	Apo-Mpro	0.25	1.3	
6	Mpro- CHEMBL 502955	0.28	1.4	3.55
7	Mpro-CHEMBL2335028	0.25	1.4	2.43
8	Mpro-CHEMBL4215430	0.30	1.4	2.36
9	Apo-PLpro	0.31	1.6	
10	PLpro-CHEMBL2288848	0.29	1.3	0.93
11.	PLpro- CHEMBL2335026	0.28	1.4	1.23
12.	PLpro-CHEMBL488913	0.32	1.5	1.06

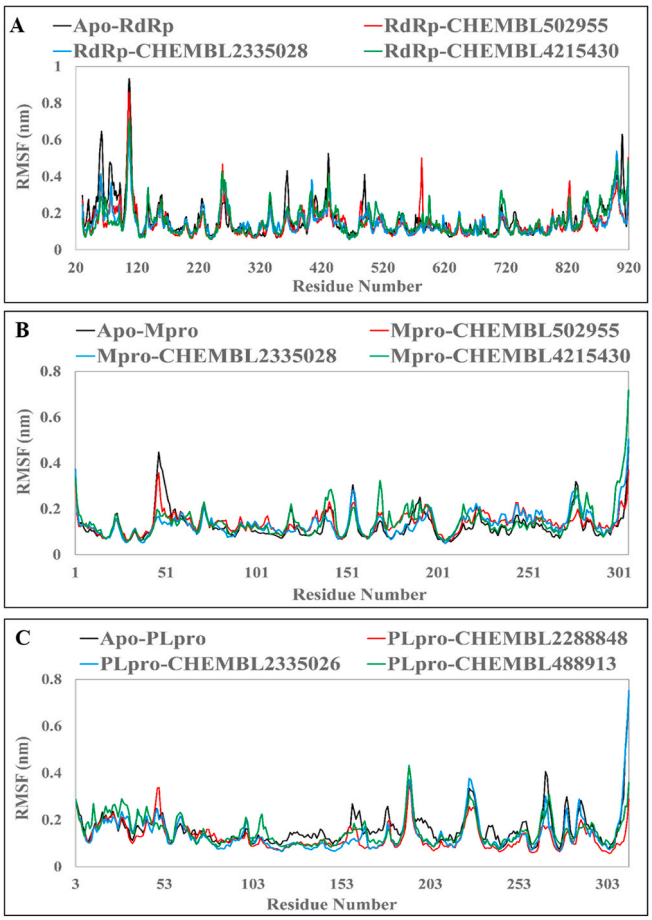

Fig. 8. RMSF graphs of: A) Apo-RdRp and RdRp-ligand complexes; B) Apo-Mpro and Mpro-ligand complexes; and C) Apo-PLpro and PLpro-ligand complexes for the duration of 50 ns of molecular dynamics.

(Fig. 7B). Mpro-CHEMBL502955, Mpro-CHEMBL2335028, and Mpro-CHEMBL4215430 complexes were stable after 20 ns with an average magnitude of deviations 0.28, 0.24, and 0.3 nm respectively, as shown in Table 3. In the case of PLpro, Apo-PLpro and the ligand-bound forms deviate by a similar extent and the deviations range between 0.2 and 0.5 nm with an average deviation of 0.32 nm and 0.28 nm respectively, as shown in Fig. 7C and Table 3.

3.3.2. *RMSF calculations*

The RMSF reflects the stability and mobility of a particular residue about its mean position. The flexibility patterns of the backbone atoms of each residue of native proteins and in complex with ligands were studied through RMSF analysis. The ligand-bound RdRp complexes were relatively more stable near the N-terminal β-hairpin (Asp29-Lys50), the nidovirus RdRp-associated nucleo-tidyltransferase (NiRAN) domain (Asp60-Arg249), and the fingers subdomain (Leu366-Ala581), and the magnitude of fluctuations were higher at the interface domain (Ala250-Arg365), the finger subdomain (Lys621-Gly679), and the palm subdomain (Thr582-Pro620, Thr680-Gln815) compared to the Apo-RdRp (Fig. 8A). The Mpro-CHEMBL502955, Mpro-CHEMBL2335028, and Mpro-CHEMBL4215430 had a stable run. The major contribution coming from the N and C-termini loops. The 3_{10} helix formed by the TSEDMLN (45–51) is more stable in protein-ligand complexes than that in Apo-Mpro (Fig. 8B). The Apo-PLpro, PLpro-CHEMBL2288848, PLpro-CHEMBL2335026, and PLpro-CHEMBL488913 showed minimal fluctuations with an average RMSF of 1.6 Å, 1.3 Å, 1.4 Å, and 1.5 Å respectively (Table 3). The Beta-Loop-2(BL2) (G266-G271) in holo form showed much lower structural flexibility and greater stability than Apo-PLpro throughout the 50 ns MD run (Fig. 8C). The RMSF values for the simulated structures are also in good qualitative agreement with that of the RMSF calculated from the experimental B-factor values (Figure S1).

3.3.3. *Hydrogen bond analysis*

Hydrogen bonding is a critical driving force defining the stability and flexibility of the ligands in protein-ligand complexes. The protein-ligand complexes are stabilized by van der Waals, electrostatic and hydrophobic interactions in addition to classical and non-classical hydrogen bonds. The number of hydrogen bonds stabilizing protein-ligand complexes were maintained throughout the 50 ns of MD run (Fig. 9). The average number of hydrogen bonds in RdRp-CHEMBL502955 (Azadirachtin-Q), RdRp-CHEMBL2335028 (Ceramicine-J), and RdRp-CHEMBL4215430 (Withanolide) were 4.55, 1.52, and 2.68, respectively. In Mpro-CHEMBL502955, Mpro-CHEMBL2335028, Mpro-CHEMBL4215430 were 3.55, 2.43, and 2.36, respectively and in

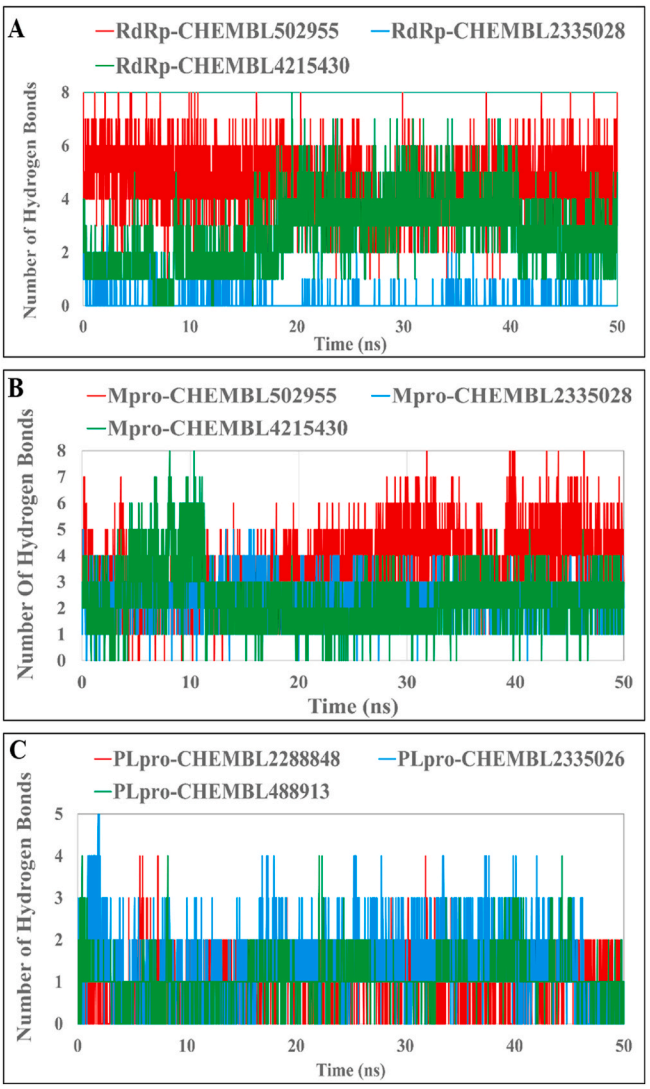

Fig. 9. Hydrogen bond analysis of azadirachtins, ceramicines, and withanolides with A) RdRp, B) Mpro, and C) PLpro, for the molecular dynamics of 50 ns.

PLpro-CHEMBL2288848 (Azadirachtin-I)PLpro-CHEMBL2335026 (Ceramicine-H), and PLpro-CHEMBL488913 (Withanolide-F) were 0.93, 1.23, and 1.06, respectively (Table 3).

3.4. Essential dynamics

The principal component analysis was carried out on the MD trajectories of apo and ligand forms of all the proteins to study the relative molecular motions of functionally significant substructures. The traces of the covariance matrix for Apo-RdRp, RdRp-CHEMBL502955, RdRp-CHEMBL2335028, RdRp-CHEMBL4215430 before diagonalization was calculated as 104.6, 75.4, 72.4, and 86.9 nm^2, respectively. Apo-PLpro, PLpro-CHEMBL2288848, PLpro-CHEMBL2335026, and PLpro-CHEMBL488913 showed as 29.9, 17.7, 24.4, and 20.5 nm^2, respectively. The plot of the first 10 eigenvalues against eigenvector indices produced by diagonalization of the covariance matrix shows that the eigenvalues of Apo-RdRp and PLpro are much higher than the ligand-bound forms. This signifies that the Apo-RdRp and PLpro are energetically less favorable and structurally more dynamic than the ligand-bound forms (Fig. 10A, Fig. 10E). These observations are supported by the plot of PCs, eigenvalues (EV1 and EV2) subjected in a phase space where the scattering of atoms in Apo-RdRp and PLpro occupy much higher conformational space than in complex with ligands (Fig. 10B and 10F). Most of the collective movements in Apo-RdRp are contributed from (NiRAN) domain (Asp60-Arg249) and the fingers subdomain (Leu366-Ala581) (Fig. 11). In Apo-PLpro, the C-terminal residues of finger subdomain (Tyr310-Lys315) are highly flexible, and the BL2 loop (Gly266-Gly271) in ligand-bound PLpro has more confined conformations, as shown in (Fig. 13). These observations are in agreement with the RMSF calculations discussed earlier. The covariance matrix in Apo-Mpro, Mpro-CHEMBL502955, Mpro-CHEMBL2335028, and Mpro-CHEMBL4215430 was 18.4, 19.7, 19.6, and 23.5 nm^2, respectively. Ligand bound Mpro has higher eigenvalues and appears to occupy a larger conformational space, the reason being the flexibility of the terminal residues in holo forms (Fig. 10C). These assumptions are well supported by the RMSF calculations (Fig. 8). Although ligand-bound Mpro appears to occupy higher conformational space, the TSEDMLN (45–51) loop is relatively more confined and stable compared to Apo-Mpro (Fig. 12).

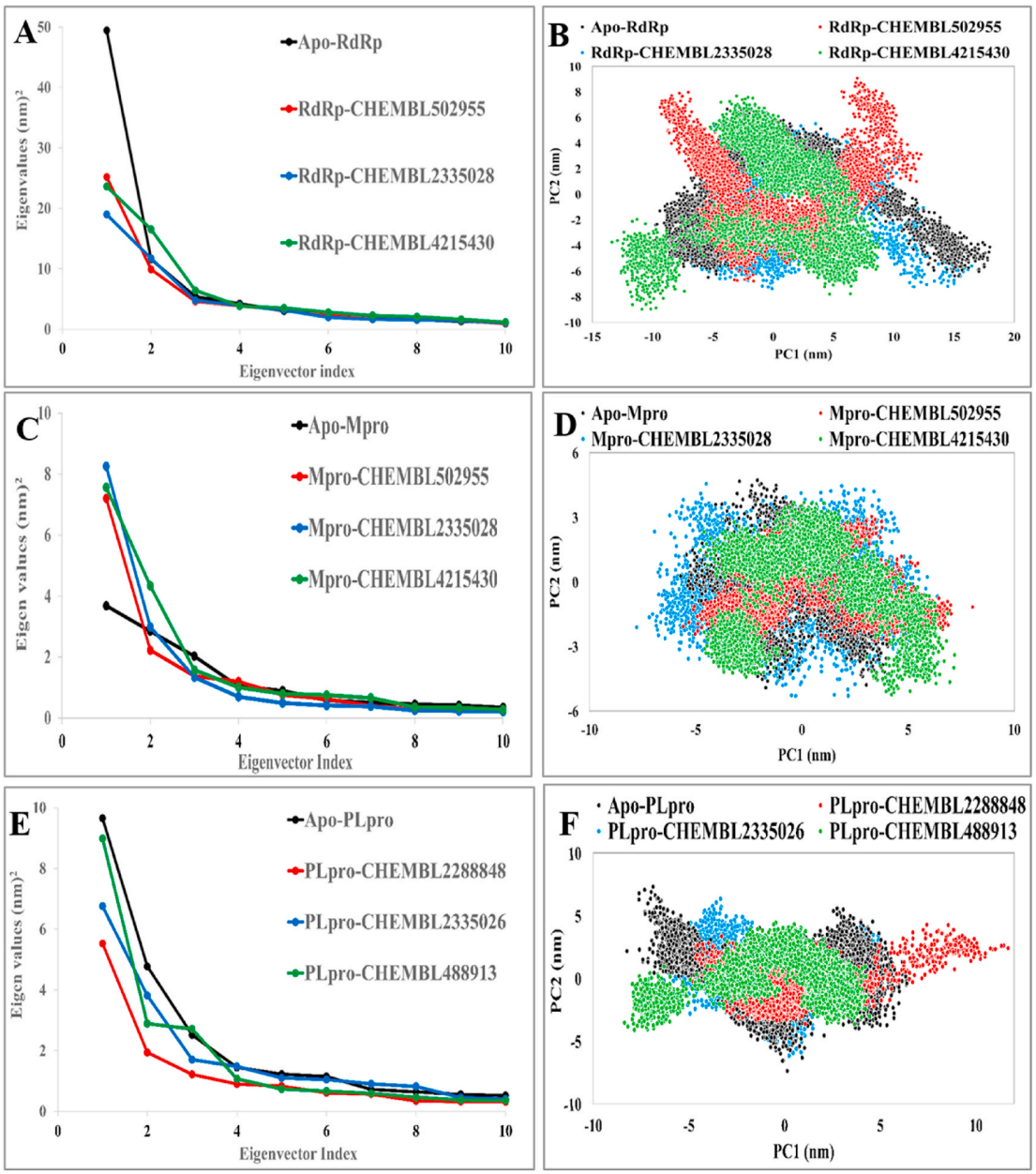

Fig. 10. Essential dynamics of RdRp, Mpro and PLpro: A, C, E) The eigenvalues plotted against their corresponding eigenvector indices obtained from the diagonalization of the covariance matrix. B,D,F) The PCA plot of Cα backbone atoms constructed by projecting the first two eigenvectors (ev1 & ev2) in the conformational space.

3.5. Binding free energy calculations using MM/PBSA

The free energy of binding of the ligands in a macromolecule-ligand complex is decided by different molecular forces like hydrogen, van der Waals, hydrophobic, electrostatic interactions between the ligand and the macromolecule. MM/PBSA calculates the aforementioned favorable forces, including solvent accessible surface area (SASA) and unfavorable polar solvation energy (PSE) [57]. The MM/PBSA computed free energy of binding for RdRp-CHEMBL502955, RdRp-CHEMBL2335028, and RdRp-CHEMBL4215430 was estimated to be −86.55 ± 51.96, −118.70 ± 29.84, and −120.46 ± 7.45 kJ/mol respectively, as shown in Table 4. For Mpro-CHEMBL502955, Mpro-CHEMBL2335028, Mpro-CHEMBL 4215430 it was calculated as −163.72 ± 15.89, −136.83 ± 19.08, −122.31 ± 31.65 kJ/mol (Table 5), PLpro-CHEMBL2288848, PLpro--CHEMBL2335026, PLPro-CHEMBL488913 showed binding affinity of −122.26 ± 28.26, −127.72 ± 47.76 and −90.04 ± 17.47 kJ/mol respectively (Table 6).

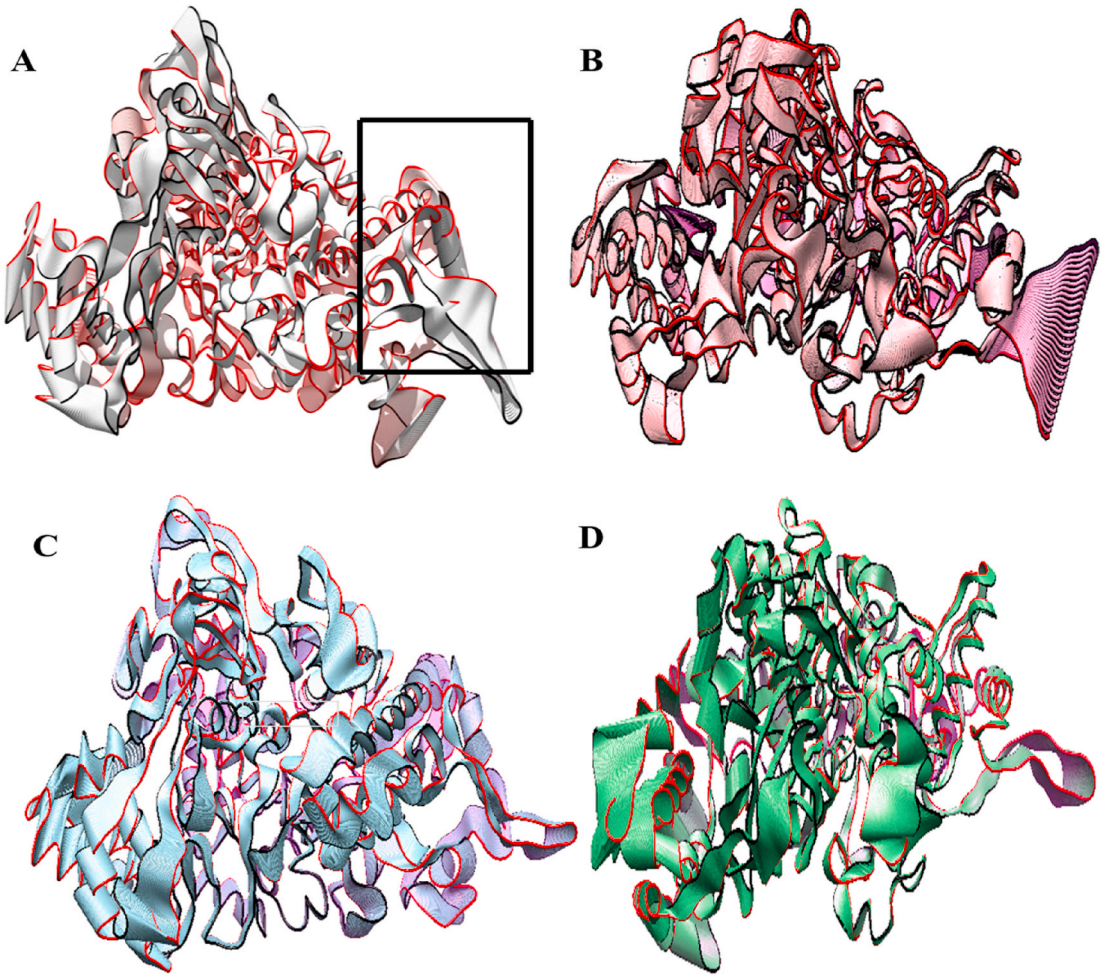

Fig. 11. A) The global motions of Apo-RdRp obtained by projection of recorded Cα movements onto the first eigenvector where rectangular box highlights the movement of NiRAN domain (60–249. The superpositioned configurations of: B) RdRp-CHEMBL502955, C) RdRp-CHEMBL2335028, and D) RdRp-CHEMBL4215430. The black ribbon is the initial configuration and the red ribbon is the final configuration during the molecular simulation. (For interpretation of the references to color in this figure legend, the reader is referred to the Web version of this article.)

4. Discussion

The medicinal properties of plants are recognized since ancient times. Triterpenoids have been extensively studied for their biological and pharmacological significance and are known to act at different stages of viral infection [59,60]. They are known to inhibit the entry of influenza A, Marburg, ebola, HCV, and HIV and also act as RTase inhibitors, protease inhibitors, maturation inhibitors, immunomodulators, and some as bifunctional inhibitors [61,62]. Salaspermic acid and Mimusopic acid inhibited HIV-RTase with an IC_{50} in micromolar concentration. Glycyrrhizic acid was shown to inhibit the replication of SARS-CoVs and Saikosaponins was shown to inhibit the replication of HCoV-22E9 (IC50 = 1.7 ± 0.1 mmol/L) [61–65]. Limonoids extracted from *Neem*, *Citrus*, Withania sominifera, and other plants are well-established antivirals and are known to inhibit the replication of human immunodeficiency virus (HIV), chikungunya, dengue virus, herpes simplex virus, and Hepatitis C Virus [21,66]. Triterpenoids like Ferruginol (IC_{50} = 49.6 μM), quinone-methide triterpenoids like celastrol (IC_{50} = 2.6 μM) pritimererin (IC_{50} = 9.9 μM), tingenone (IC_{50} = 5.5 μM), and iguesterin (IC_{50} = 10.3 μM), betulinic acid (Ki = 8.2 ± 0.7 μM) showed inhibitory activities against SARS-CoVs Mpro [67–69]. These compounds are abundantly present in citrus fruits like lemons, oranges, grapefruits. Hence are readily available and can be taken up directly from the plant source or can also be used as a nutraceutical formulation [17,70,71].

The studied compounds when screened against SARS-CoV-2 RdRp, Mpro, and PLpro, were estimated to bind at the RdRp catalytic site 'SDD' (759–761) involving Lys545, Arg553, and Arg555 residues that make up the NTP entry site and Asp623 in motif A, that interrogates the 3′OH of the incoming nucleotide. The Mpro-ligand complexes involve the catalytic triad formed by Met49, Cys145, and Gln189. In the case of PLpro, the PLpro-ligand docked complexes involve the hydrophobic pocket formed by Pro247, Pro248, Tyr264, Tyr268, and Thr301. The protein-ligand complexes remain stable for the 50 ns of MD run with a binding energy of −86.5 to −163.7 kJ/mol while maintaining the minimum number of hydrogen bonds. The principal component analysis reveals that the atoms in ligand-bound complexes are scattered in a lower conformational space and are relatively much stable and less dynamic than the apo structures. These compounds could be of therapeutic importance in context to SARS-

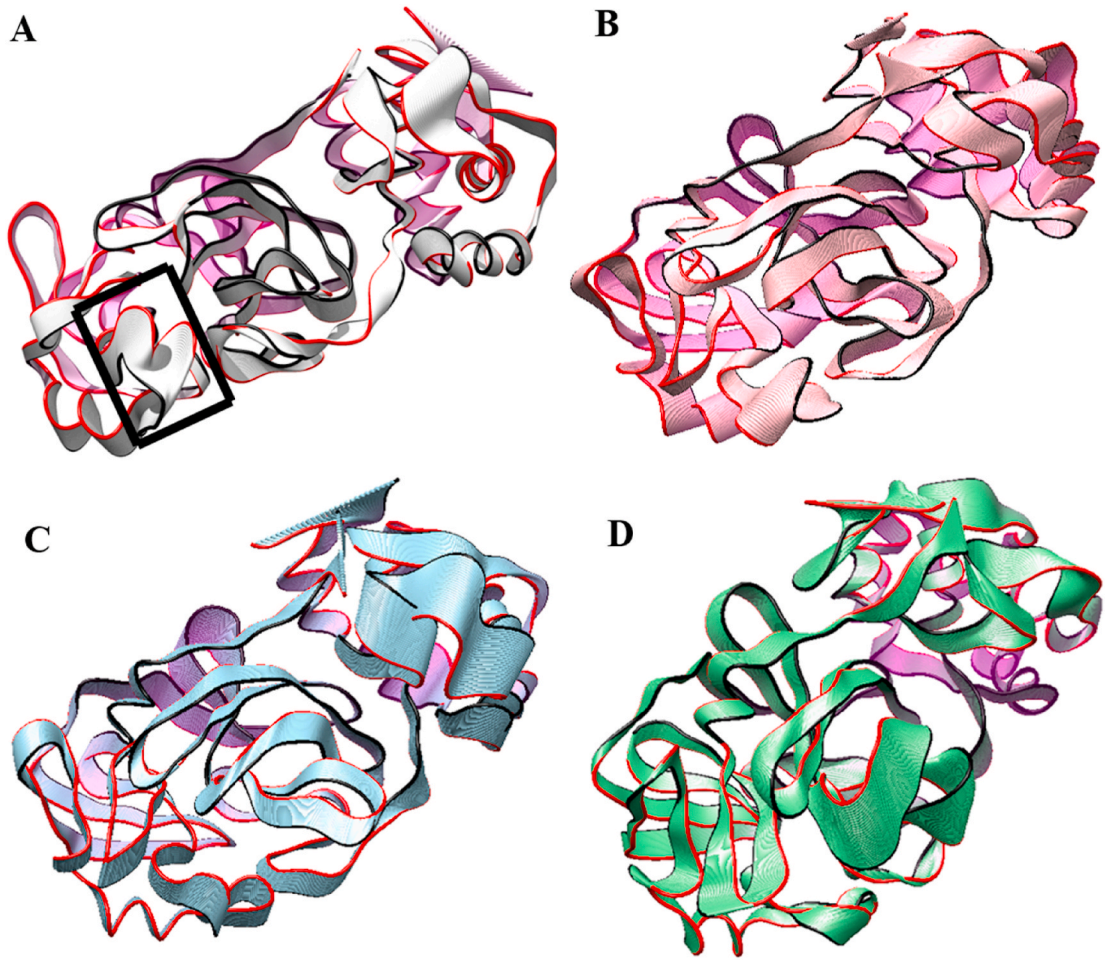

Fig. 12. A) The overall motions of Apo-Mpro recorded over time by projecting Cα movements along the first eigenvector and final structure. The initial configuration (black color) is superpositioned to the final structure (red color) and TSEDMLN loop (45–51) movements are highlighted in the rectangle. The overall motions of Mpro-CHEMBL502955 (B), Mpro-CHEMBL2335028 (C), and Mpro- CHEMBL4215430 (D) are shown in cartoon representation. (For interpretation of the references to color in this figure legend, the reader is referred to the Web version of this article.)

CoV-2 treatment because of their anti-inflammatory properties to counter the cytokine storm [7,11–14]. They modulate pathways that are essential to establish persistent infection and pathogenesis of SARS-CoV-2 and are also known to inhibit cathepsin-L, which is critical for the entry of SARS-CoV-2 [18,19,21]. They are reported to inhibit cytoprotective autophagy and promote apoptosis of infected cells [20,25,72,73]. The aforementioned properties of these compounds satisfy their role in combating the spectrum of diseases followed by SARS-CoV-2 infection. The inhibitory potential of these compounds in context to SARS-CoV-2 RdRp, Mpro, and PLpro deserves further experimental attention.

Disclosure statement

No conflict of interest is reported by the authors.

Author contributions

K Amith Kumar- Conceptualization, Investigation, Formal analysis, Writing - original draft preparation.

Monica Sharma - Formal analysis, Writing - original draft preparation.

Vikram Dalal- Writing - original draft preparation.

Vishakha Singh- Writing - original draft preparation.

Shailly Tomar- Conceptualization, Supervision, Funding acquisition.

Pravindra Kumar - Conceptualization, Supervision, Resources, Funding acquisition, Writing - review & editing.

Declaration of competing interest

The authors declare that they have no known competing financial interests or personal relationships that could have appeared to influence the work reported in this paper.

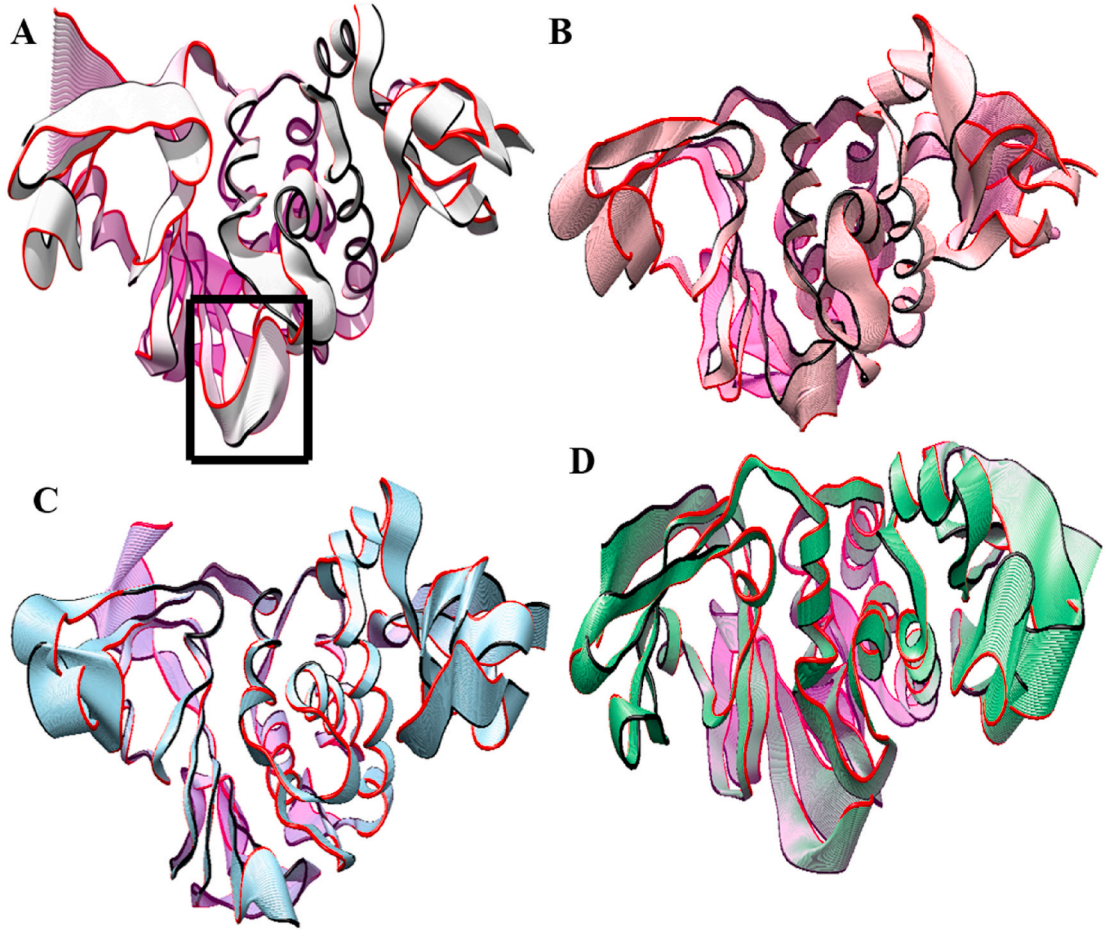

Fig. 13. A) The global motions of Cα in Apo-PLpro along the first eigenvector where the initial configuration in the superpositioned structures is colored in black and the final structure is colored as red. The overall motions of Cα in PLpro-CHEMBL2288848 (B), PLpro-CHEMBL2335026 (C), and PLpro-CHEMBL488913 (D). (For interpretation of the references to color in this figure legend, the reader is referred to the Web version of this article.)

Table 4
Binding free energy (kJ/mol) of RdRp-CHEMBL502955, RdRp-CHEMBL2335028, and RdRp-CHEMBL4215430 complexes calculated by MM/PBSA. All the binding affinities were calculated using 1000 frames from the last 10 ns (40–50 ns) of molecular dynamics simulation.

Energy (kJ/mol)	CHEMBL502955	CHEMBL2335028	CHEMBL4215430
Van der Waal energy	−213.34 ± 18.82	−170.91 ± 5.53	−203.61 ± 8.74
Electrostatic energy	−87.18 ± 27.93	−28.62 ± 20.91	−131.20 ± 8.45
Polar solvation energy	233.27 ± 61.53	96.68 ± 51.00	233.54 ± 13.07
SASA energy	−19.29 ± 0.48	−15.46 ± 1.02	−18.84 ± 0.50
Binding energy	−86.55 ± 51.96	−118.70 ± 29.84	−120.46 ± 7.45

Table 5
MM/PBSA free energy calculations of Mpro-CHEMBL502955, Mpro-CHEMBL2335028, and Mpro-CHEMBL4215430 complexes.

Energy (kJ/mol)	CHEMBL502955	CHEMBL2335028	CHEMBL4215430
Van der Waal energy	−241.14 ± 24.26	−200.72 ± 20.25	−167.50 ± 34.71
Electrostattic energy	−51.74 ± 9.33	−33.97 ± 8.15	−37.11 ± 9.33
Polar solvation energy	149.14 ± 7.638	114.42 ± 10.63	96.09 ± 13.70
SASA energy	−19.99 ± 0.165	−16.56 ± 1.27	−13.32 ± 2.81
Binding energy	−163.72 ± 15.89	−136.83 ± 19.08	−122.31 ± 31.65

Table 6
Binding free energy calculation of PLpro-CHEMBL228848, PLpro-CHEMBL2335026, and PLpro-CHEMBL488913 complexes using MM/PBSA.

Energy (kJ/mol)	CHEMBL2288848	CHEMBL2335026	CHEMBL488913
Van der Waal energy	−181.953 ± 30.41	−158.95 ± 74.05	−113.25 ± 21.23
Electrostattic energy	−19.032 ± 4.57	−26.34 ± 17.74	−9.50 ± 4.42
Polar solvation energy	95.021 ± 14.94	71.14 ± 45.78	41.79 ± 10.54
SASA energy	−16.30 ± 1.13	−13.55 ± 5.61	−9.254 ± 2.08
Binding energy	−122.26 ± 28.26	−127.72 ± 47.76	−90.04 ± 17.47

Acknowledgements

Authors would like to acknowledge Science and Engineering Research Board, Department of Science & Technology, Government of India [DST-SERB IPA/2020/000054]. A.K, M.S, V. D, and V.S would like to thank CSIR, MHRD, DBT, and ICMR, respectively for providing financial assistance. Authors would like to pay sincere thanks to Macromolecular Crystallographic Unit (MCU), a Central Facility at Institute Instrumentation Center (IIC), IIT Roorkee for providing lab facilities.

Appendix A. Supplementary data

Supplementary data to this article can be found online at https://doi.org/10.1016/j.jmgm.2021.107969.

References

[1] R. Mudgal, S. Nehul, S. Tomar, Prospects for mucosal vaccine: shutting the door on SARS-CoV-2, Hum. Vaccines Immunother. 16 (2020) 2921–2931, https://doi.org/10.1080/21645515.2020.1805992.
[2] D.A.J. Tyrrell, S.H. Myint, Coronaviruses, in: S. Baron (Ed.), Med. Microbiol., fourth ed., University of Texas Medical Branch at Galveston, Galveston (TX), 1996. http://www.ncbi.nlm.nih.gov/books/NBK7782/. (Accessed 20 November 2020).
[3] B. Chen, E.-K. Tian, B. He, L. Tian, R. Han, S. Wang, Q. Xiang, S. Zhang, T. El Arnaout, W. Cheng, Overview of lethal human coronaviruses, Signal Transduct. Target. Ther. 5 (2020) 89, https://doi.org/10.1038/s41392-020-0190-2.
[4] Y. Lim, Y. Ng, J. Tam, D. Liu, Human coronaviruses: a review of virus–host interactions, Diseases 4 (2016) 26, https://doi.org/10.3390/diseases4030026.
[5] R. Carrasco-Hernandez, R. Jácome, Y. López Vidal, S. Ponce de León, Are RNA viruses candidate agents for the next global pandemic? A Review, ILAR J. 58 (2017) 343–358, https://doi.org/10.1093/ilar/ilx026.
[6] R.J. Jose, A. Manuel, COVID-19 cytokine storm: the interplay between inflammation and coagulation, Lancet Respir. Med. 8 (2020) e46–e47, https://doi.org/10.1016/S2213-2600(20)30216-2.
[7] P. Sarzi-Puttini, V. Giorgi, S. Sirotti, D. Marotto, S. Ardizzone, G. Rizzardini, S. Antinori, M. Galli, COVID-19, cytokines and immunosuppression: what can we learn from severe acute respiratory syndrome? Clin. Exp. Rheumatol. (2020) 6.
[8] S. Molaei, M. Dadkhah, V. Asghariazar, C. Karami, E. Safarzadeh, The immune response and immune evasion characteristics in SARS-CoV, MERS-CoV, and SARS-CoV-2: vaccine design strategies, Int. Immunopharm. 92 (2021) 107051, https://doi.org/10.1016/j.intimp.2020.107051.
[9] M. Catanzaro, F. Fagiani, M. Racchi, E. Corsini, S. Govoni, C. Lanni, Immune response in COVID-19: addressing a pharmacological challenge by targeting pathways triggered by SARS-CoV-2, Signal Transduct. Target, Therapy 5 (2020) 84, https://doi.org/10.1038/s41392-020-0191-1.
[10] M. Jamal, H.I. Bangash, M. Habiba, Y. Lei, T. Xie, J. Sun, Z. Wei, Z. Hong, L. Shao, Q. Zhang, Immune dysregulation and system pathology in COVID-19, Virulence, 12, https://doi.org/10.1080/21505594.2021.1898790, 2021, 918-936.
[11] L. Yang, S. Liu, J. Liu, Z. Zhang, X. Wan, B. Huang, Y. Chen, Y. Zhang, COVID-19: immunopathogenesis and Immunotherapeutics, Signal Transduct. Target. Ther. 5 (2020) 128, https://doi.org/10.1038/s41392-020-00243-2.
[12] T. Akihisa, T. Noto, A. Takahashi, Y. Fujita, N. Banno, H. Tokuda, K. Koike, T. Suzuki, K. Yasukawa, Y. Kimura, Melanogenesis inhibitory, anti-inflammatory, and chemopreventive effects of limonoids from the seeds of azadirachta indicia A. Juss. (Neem), J. Oleo Sci. 58 (2009) 581–594, https://doi.org/10.5650/jos.58.581.
[13] C. Sarigaputi, D. Sommit, T. Teerawatananond, K. Pudhom, Weakly anti-inflammatory limonoids from the seeds of *Xylocarpus rumphii*, J. Nat. Prod. 77 (2014) 2037–2043, https://doi.org/10.1021/np5003687.
[14] Y. Zhang, H. Xu, Recent progress in the chemistry and biology of limonoids, RSC Adv. 7 (2017) 35191–35220, https://doi.org/10.1039/C7RA04715K.
[15] M.A. Alzohairy, Therapeutics role of *Azadirachta indica* (neem) and their active constituents in diseases prevention and treatment, evid. Based complement, Alternative Med. 2016 (2016) 1–11, https://doi.org/10.1155/2016/7382506.
[16] G. Sanna, S. Madeddu, G. Giliberti, N.G. Ntalli, F. Cottiglia, A. De Logu, E. Agus, P. Caboni, Limonoids from melia azedarach fruits as inhibitors of flaviviruses and Mycobacterium tubercolosis, PloS One 10 (2015), e0141272, https://doi.org/10.1371/journal.pone.0141272.
[17] R. Tundis, M.R. Loizzo, F. Menichini, An overview on chemical aspects and potential health benefits of limonoids and their derivatives, Crit. Rev. Food Sci. Nutr. 54 (2014) 225–250, https://doi.org/10.1080/10408398.2011.581400.
[18] Suelem D. Ramalho, Lorena R.F. DeSousa, L. Nebo, Stella H. Maganhi, I. Caracelli, J. Zukerman-Schpector, Maria I.S. Lima, Marcio F.M. Alves, M. Fátima das G. F. DaSilva, João B. Fernandes, Paulo C. Vieira, Triterpenoids as novel natural inhibitors of human cathepsin L,, Chem. Biodivers. 11 (2014) 1354–1363, https://doi.org/10.1002/cbdv.201400065.
[19] G. Simmons, D.N. Gosalia, A.J. Rennekamp, J.D. Reeves, S.L. Diamond, P. Bates, Inhibitors of cathepsin L prevent severe acute respiratory syndrome coronavirus entry, Proc. Natl. Acad. Sci. Unit. States Am. 102 (2005) 11876–11881, https://doi.org/10.1073/pnas.0505577102.
[20] Z. Wang, X. Cheng, Q. Meng, P. Wang, B. Shu, Q. Hu, M. Hu, G. Zhong, Azadirachtin-induced apoptosis involves lysosomal membrane permeabilization and cathepsin L release in Spodoptera frugiperda Sf9 cells, Int. J. Biochem. Cell Biol. 64 (2015) 126–135, https://doi.org/10.1016/j.biocel.2015.03.018.
[21] P.R. Sudhakaran (Ed.), Perspectives in Cancer Prevention-Translational Cancer Research, Springer India, New Delhi, 2014, https://doi.org/10.1007/978-81-322-1533-2.
[22] M. Thoh, P. Kumar, H.A. Nagarajaram, S.K. Manna, Azadirachtin interacts with the tumor necrosis factor (TNF) binding domain of its receptors and inhibits TNF-induced biological responses, J. Biol. Chem. 287 (2012), https://doi.org/10.1074/jbc.A109.065847, 13556–13556.
[23] T. Mizutani, S. Fukushi, M. Saijo, I. Kurane, S. Morikawa, JNK and PI3k/Akt signaling pathways are required for establishing persistent SARS-CoV infection in Vero E6 cells, Biochim. Biophys. Acta BBA - Mol. Basis Dis. 1741 (2005) 4–10, https://doi.org/10.1016/j.bbadis.2005.04.004.
[24] Z. Wehbe, S. Hammoud, N. Soudani, H. Zaraket, A. El-Yazbi, A.H. Eid, Molecular insights into SARS COV-2 interaction with cardiovascular disease: role of RAAS and MAPK signaling, Front. Pharmacol. 11 (2020) 836, https://doi.org/10.3389/fphar.2020.00836.
[25] T. Mizutani, S. Fukushi, M. Saijo, I. Kurane, S. Morikawa, Importance of Akt signaling pathway for apoptosis in SARS-CoV-infected Vero E6 cells, Virology 327 (2004) 169–174, https://doi.org/10.1016/j.virol.2004.07.005.
[26] T. Mizutani, S. Fukushi, K. Ishii, Y. Sasaki, T. Kenri, M. Saijo, Y. Kanaji, K. Shirota, I. Kurane, S. Morikawa, Mechanisms of establishment of persistent SARS-CoV-infected cells, Biochem. Biophys. Res. Commun. 347 (2006) 261–265, https://doi.org/10.1016/j.bbrc.2006.06.086.
[27] T.S. Fung, D.X. Liu, Human coronavirus: host-pathogen interaction, Annu. Rev. Microbiol. 73 (2019) 529–557, https://doi.org/10.1146/annurev-micro-020518-115759.
[28] C.-H. Wu, S.-H. Yeh, Y.-G. Tsay, Y.-H. Shieh, C.-L. Kao, Y.-S. Chen, S.-H. Wang, T.-J. Kuo, D.-S. Chen, P.-J. Chen, Glycogen synthase kinase-3 regulates the phosphorylation of severe acute respiratory syndrome coronavirus nucleocapsid protein and viral replication, J. Biol. Chem. 284 (2009) 5229–5239, https://doi.org/10.1074/jbc.M805747200.
[29] J. Sophia, J. Kowshik, A. Dwivedi, S.K. Bhutia, B. Manavathi, R. Mishra, S. Nagini, Nimbolide, a neem limonoid inhibits cytoprotective autophagy to activate apoptosis via modulation of the PI3K/Akt/GSK-3β signalling pathway in oral cancer, Cell Death Dis. 9 (2018) 1087, https://doi.org/10.1038/s41419-018-1126-4.
[30] S.M. Poulose, E.D. Harris, B.S. Patil, Citrus limonoids induce apoptosis in human neuroblastoma cells and have radical scavenging activity, J. Nutr. 135 (2005) 870–877, https://doi.org/10.1093/jn/135.4.870.
[31] A.M. Zaki, S. van Boheemen, T.M. Bestebroer, A.D.M.E. Osterhaus, R.A. M. Fouchier, Isolation of a novel coronavirus from a man with pneumonia in Saudi arabia, N. Engl. J. Med. 367 (2012) 1814–1820, https://doi.org/10.1056/NEJMoa1211721.
[32] S. van Boheemen, M. de Graaf, C. Lauber, T.M. Bestebroer, V.S. Raj, A.M. Zaki, A.D. M.E. Osterhaus, B.L. Haagmans, A.E. Gorbalenya, E.J. Snijder, R.A.M. Fouchier, Genomic characterization of a newly discovered coronavirus associated with acute respiratory distress syndrome in humans, mBio 3 (2012), https://doi.org/10.1128/mBio.00473-12 e00473-12.
[33] S. Payne, Family Coronaviridae, in: Viruses, Elsevier, 2017, pp. 149–158, https://doi.org/10.1016/B978-0-12-803109-4.00017-9.
[34] S. Dallakyan, A.J. Olson, Small-molecule library screening by docking with PyRx, in: J.E. Hempel, C.H. Williams, C.C. Hong (Eds.), Chem. Biol, Springer, New York, New York, NY, 2015, pp. 243–250, https://doi.org/10.1007/978-1-4939-2269-7_19.
[35] G.M. Morris, R. Huey, A.J. Olson, Using AutoDock for ligand-receptor docking, Curr. Protoc. Bioinforma. 24 (2008), https://doi.org/10.1002/0471250953.bi0814s24.

[36] A. Waterhouse, M. Bertoni, S. Bienert, G. Studer, G. Tauriello, R. Gumienny, F. T. Heer, T.A.P. de Beer, C. Rempfer, L. Bordoli, R. Lepore, T. Schwede, SWISS-MODEL: homology modelling of protein structures and complexes, Nucleic Acids Res. 46 (2018) W296–W303, https://doi.org/10.1093/nar/gky427.
[37] Y. Gao, L. Yan, Y. Huang, F. Liu, Y. Zhao, L. Cao, T. Wang, Q. Sun, Z. Ming, L. Zhang, J. Ge, L. Zheng, Y. Zhang, H. Wang, Y. Zhu, C. Zhu, T. Hu, T. Hua, B. Zhang, X. Yang, J. Li, H. Yang, Z. Liu, W. Xu, L.W. Guddat, Q. Wang, Z. Lou, Z. Rao, Structure of the RNA-dependent RNA polymerase from COVID-19 virus, Science 368 (2020) 779–782, https://doi.org/10.1126/science.abb7498.
[38] Z. Jin, X. Du, Y. Xu, Y. Deng, M. Liu, Y. Zhao, B. Zhang, X. Li, L. Zhang, C. Peng, Y. Duan, J. Yu, L. Wang, K. Yang, F. Liu, R. Jiang, X. Yang, T. You, X. Liu, X. Yang, F. Bai, H. Liu, X. Liu, L.W. Guddat, W. Xu, G. Xiao, C. Qin, Z. Shi, H. Jiang, Z. Rao, H. Yang, Structure of Mpro from SARS-CoV-2 and discovery of its inhibitors, Nature 582 (2020) 289–293, https://doi.org/10.1038/s41586-020-2223-y.
[39] R. Pokhrel, P. Chapagain, J. Siltberg-Liberles, Potential RNA-dependent RNA polymerase inhibitors as prospective therapeutics against SARS-CoV-2, J. Med. Microbiol. 69 (2020) 864–873, https://doi.org/10.1099/jmm.0.001203.
[40] S. Günther, P.Y.A. Reinke, Y. Fernández-García, J. Lieske, T.J. Lane, H.M. Ginn, F. H.M. Koua, C. Ehrt, W. Ewert, D. Oberthuer, O. Yefanov, S. Meier, K. Lorenzen, B. Krichel, J.-D. Kopicki, L. Gelisio, W. Brehm, I. Dunkel, B. Seychell, H. Gieseler, B. Norton-Baker, B. Escudero-Pérez, M. Domaracky, S. Saouane, A. Tolstikova, T. A. White, A. Hänle, M. Groessler, H. Fleckenstein, F. Trost, M. Galchenkova, Y. Gevorkov, C. Li, S. Awel, A. Peck, M. Barthelmess, F. Schlünzen, P. Lourdu Xavier, N. Werner, H. Andaleeb, N. Ullah, S. Falke, V. Srinivasan, B.A. França, M. Schwinzer, H. Brognaro, C. Rogers, D. Melo, J.J. Zaitseva-Doyle, J. Knoska, G. E. Peña-Murillo, A.R. Mashhour, V. Hennicke, P. Fischer, J. Hakanpää, J. Meyer, P. Gribbon, B. Ellinger, M. Kuzikov, M. Wolf, A.R. Beccari, G. Bourenkov, D. von Stetten, G. Pompidor, I. Bento, S. Panneerselvam, I. Karpics, T.R. Schneider, M. M. Garcia-Alai, S. Niebling, C. Günther, C. Schmidt, R. Schubert, H. Han, J. Boger, D.C.F. Monteiro, L. Zhang, X. Sun, J. Pletzer-Zelgert, J. Wollenhaupt, C.G. Feiler, M.S. Weiss, E.-C. Schulz, P. Mehrabi, K. Karničar, A. Usenik, J. Loboda, H. Tidow, A. Chari, R. Hilgenfeld, C. Uetrecht, R. Cox, A. Zaliani, T. Beck, M. Rarey, S. Günther, D. Turk, W. Hinrichs, H.N. Chapman, A.R. Pearson, C. Betzel, A. Meents, X-ray screening identifies active site and allosteric inhibitors of SARS-CoV-2 main protease, Science 372 (2021) 642–646, https://doi.org/10.1126/science.abf7945.
[41] Systèmes, Dassault Biovia Discovery Studio, Dassault Syst Mes BIOVIA, Discovery Studio Modeling Environment, Release 2017, Dassault Syst mes, 2016 n.d.
[42] H.J.C. Berendsen, D. van der Spoel, R. van Drunen, GROMACS: a message-passing parallel molecular dynamics implementation, Comput. Phys. Commun. 91 (1995) 43–56, https://doi.org/10.1016/0010-4655(95)00042-E.
[43] M.J. Abraham, T. Murtola, R. Schulz, S. Páll, J.C. Smith, B. Hess, E. Lindahl, GROMACS: high performance molecular simulations through multi-level parallelism from laptops to supercomputers, Software 1–2 (2015) 19–25, https://doi.org/10.1016/j.softx.2015.06.001.
[44] L.D. Schuler, X. Daura, W.F. van Gunsteren, An improved GROMOS96 force field for aliphatic hydrocarbons in the condensed phase, J. Comput. Chem. 22 (2001) 1205–1218, https://doi.org/10.1002/jcc.1078.
[45] D.M.F. van Aalten, R. Bywater, J.B.C. Findlay, M. Hendlich, R.W.W. Hooft, G. Vriend, PRODRG, a program for generating molecular topologies and unique molecular descriptors from coordinates of small molecules, J. Comput. Aided Mol. Des. 10 (1996) 255–262, https://doi.org/10.1007/BF00355047.
[46] T. Darden, D. York, L. Pedersen, Particle mesh Ewald: an $N \cdot \log(N)$ method for Ewald sums in large systems, J. Chem. Phys. 98 (1993) 10089–10092, https://doi.org/10.1063/1.464397.
[47] W.F. Van Gunsteren, H.J.C. Berendsen, A leap-frog algorithm for stochastic dynamics, Mol. Simulat. 1 (1988) 173–185, https://doi.org/10.1080/08927028808080941.
[48] G. Bussi, D. Donadio, M. Parrinello, Canonical sampling through velocity rescaling, J. Chem. Phys. 126 (2007), 014101, https://doi.org/10.1063/1.2408420.
[49] M. Parrinello, A. Rahman, Polymorphic transitions in single crystals: a new molecular dynamics method, J. Appl. Phys. 52 (1981) 7182–7190, https://doi.org/10.1063/1.328693.
[50] B. Hess, H. Bekker, H.J.C. Berendsen, LINCS: a linear constraint solver for molecular simulations, J. Comput. Chem. 18 (n.d.) 10.
[51] H. Grubmüller, H. Heller, A. Windemuth, K. Schulten, Generalized verlet algorithm for efficient molecular dynamics simulations with long-range interactions, Mol. Simulat. 6 (1991) 121–142, https://doi.org/10.1080/08927029108022142.
[52] M.M.H. Graf, U. Bren, D. Haltrich, C. Oostenbrink, Molecular dynamics simulations give insight into d-glucose dioxidation at C2 and C3 by Agaricus meleagris pyranose dehydrogenase, J. Comput. Aided Mol. Des. 27 (2013) 295–304, https://doi.org/10.1007/s10822-013-9645-7.
[53] K. Pearson, LIII. On lines and planes of closest fit to systems of points in space, Lond. Edinb. Dublin Philos. Mag. J. Sci. 2 (1901) 559–572, https://doi.org/10.1080/14786440109462720.
[54] H. Hotelling, Analysis of a complex of statistical variables into principal components, J. Educ. Psychol. 24 (1933) 417, https://doi.org/10.1037/h0071325, 19340101.
[55] g_mmpbsa, n.d. https://rashmikumari.github.io/g_mmpbsa/single_protein_ligand_binding_energy.html. (Accessed 8 May 2021).
[56] R. Kumari, R. Kumar, Open source drug discovery consortium, A. Lynn, *g_mmpbsa*—a GROMACS tool for high-throughput MM-PBSA calculations, J. Chem. Inf. Model. 54 (2014) 1951–1962, https://doi.org/10.1021/ci500020m.
[57] S. Genheden, U. Ryde, The MM/PBSA and MM/GBSA methods to estimate ligand-binding affinities, Expet Opin. Drug Discov. 10 (2015) 449–461, https://doi.org/10.1517/17460441.2015.1032936.
[58] M. Jukič, D. Janežič, U. Bren, Ensemble docking coupled to linear interaction energy calculations for identification of coronavirus main protease (3CLpro) non-covalent small-molecule inhibitors, Molecules 25 (2020) 5808, https://doi.org/10.3390/molecules25245808.
[59] A. Alqahtani, K. Hamid, A. Kam, K.H. Wong, Z. Abdelhak, V. Razmovski-Naumovski, K. Chan, K.M. Li, P.W. Groundwater, G.Q. Li, The pentacyclic triterpenoids in herbal medicines and their pharmacological activities in diabetes and diabetic complications, Curr. Med. Chem. 20 (2013) 908–931, https://doi.org/10.2174/092986713805219082.
[60] P. Dzubak, M. Hajduch, D. Vydra, A. Hustova, M. Kvasnica, D. Biedermann, L. Markova, M. Urban, J. Sarek, Pharmacological activities of natural triterpenoids and their therapeutic implications, Nat. Prod. Rep. 23 (2006) 394, https://doi.org/10.1039/b515312n.
[61] S. Xiao, Z. Tian, Y. Wang, L. Si, L. Zhang, D. Zhou, Recent progress in the antiviral activity and mechanism study of pentacyclic triterpenoids and their derivatives, Med. Res. Rev. 38 (2018) 951–976, https://doi.org/10.1002/med.21484.
[62] B.K. Cassels, M. Asencio, Anti-HIV activity of natural triterpenoids and hemisynthetic derivatives 2004–2009, Phytochemistry Rev. 10 (2011) 545–564, https://doi.org/10.1007/s11101-010-9172-2.
[63] B. Adhikari, B.P. Marasini, B. Rayamajhee, B.R. Bhattarai, G. Lamichhane, K. Khadayat, A. Adhikari, S. Khanal, N. Parajuli, Potential roles of medicinal plants for the treatment of viral diseases focusing on COVID -19: a review, Phytother Res. (2020) ptr.6893, https://doi.org/10.1002/ptr.6893.
[64] J. Shawon, Z. Akter, MdM. Hossen, Y. Akter, A. Sayeed, Md Junaid, S.S. Afrose, MdA. Khan, Current landscape of natural products against coronaviruses: perspectives in COVID-19 treatment and anti-viral mechanism, Curr. Pharmaceut. Des. 26 (2020) 5241–5260, https://doi.org/10.2174/1381612826666201106093912.
[65] K.C. Chinsembu, Chemical diversity and activity profiles of HIV-1 reverse transcriptase inhibitors from plants, Rev. Bras. Farmacogn. 29 (2019) 504–528, https://doi.org/10.1016/j.bjp.2018.10.006.
[66] A. Roy, S. Saraf, Limonoids: overview of significant bioactive triterpenes distributed in plants kingdom, Biol. Pharm. Bull. 29 (2006) 191–201, https://doi.org/10.1248/bpb.29.191.
[67] T. Pillaiyar, M. Manickam, V. Namasivayam, Y. Hayashi, S.-H. Jung, An overview of severe acute respiratory syndrome–coronavirus (SARS-CoV) 3CL protease inhibitors: peptidomimetics and small molecule chemotherapy, J. Med. Chem. (2016) 34.
[68] I.E. Orhan, F.S. Senol Deniz, Natural products as potential leads against coronaviruses: could they be encouraging structural models against SARS-CoV-2? Nat. Prod. Bioprospecting. 10 (2020) 171–186, https://doi.org/10.1007/s13659-020-00250-4.
[69] A.M. Sayed, A.R. Khattab, A.M. AboulMagd, H.M. Hassan, M.E. Rateb, H. Zaid, U. R. Abdelmohsen, Nature as a treasure trove of potential anti-SARS-CoV drug leads: a structural/mechanistic rationale, RSC Adv. 10 (2020) 19790–19802, https://doi.org/10.1039/D0RA04199H.
[70] Y.-S. Shi, Y. Zhang, H.-T. Li, C.-H. Wu, H.R. El-Seedi, W.-K. Ye, Z.-W. Wang, C.-B. Li, X.-F. Zhang, G.-Y. Kai, Limonoids from Citrus: chemistry, anti-tumor potential, and other bioactivities, J. Funct. Foods. 75 (2020) 104213, https://doi.org/10.1016/j.jff.2020.104213.
[71] R. Gualdani, M. Cavalluzzi, G. Lentini, S. Habtemariam, The chemistry and pharmacology of citrus limonoids, Molecules 21 (2016) 1530, https://doi.org/10.3390/molecules21111530.
[72] J. Sophia, J. Kowshik, A. Dwivedi, S.K. Bhutia, B. Manavathi, R. Mishra, S. Nagini, Nimbolide, a neem limonoid inhibits cytoprotective autophagy to activate apoptosis via modulation of the PI3K/Akt/GSK-3β signalling pathway in oral cancer, Cell Death Dis. 9 (2018) 1087, https://doi.org/10.1038/s41419-018-1126-4.
[73] S.M. Poulose, E.D. Harris, B.S. Patil, Citrus limonoids induce apoptosis in human neuroblastoma cells and have radical scavenging activity, J. Nutr. 135 (2005) 870–877, https://doi.org/10.1093/jn/135.4.870.